European Polymer Journal 116 (2019) 201–209

Contents lists available at ScienceDirect

European Polymer Journal

journal homepage: www.elsevier.com/locate/europolj

Gradient supramolecular interactions and tunable mechanics in polychaete jaw inspired semi-interpenetrating networks

Chase B. Thompson[a], Sourav Chatterjee[a], LaShanda T.J. Korley[a,b,*]

[a] Department of Materials Science and Engineering, University of Delaware, 127 The Green, Newark, DE 19716, USA
[b] Department of Chemical and Biomolecular Engineering, University of Delaware, 150 Academy St, Newark, DE 19716, USA

ARTICLE INFO

Keywords:
Supramolecular chemistry
Semi-interpenetrating network
Tunable mechanics
Interaction localization

ABSTRACT

Polychaete worms display a remarkable jaw structure, where a gradient in metal-ligand coordination down the length of the jaw results in a shift from hard to soft mechanics. To mimic these gradient structures, a Zn-coordinated supramolecular polymer is crosslinked into a covalent matrix to afford supramolecular semi-interpenetrating networks (SIPNs). These SIPN materials exhibit improved mechanics with a lower supramolecular content (30 wt%), allowing for energy dissipation through cavitation to increase material toughness. The shift in mechanical behavior is further attributed to the morphology, where the size of the phase-separated droplets and nature of the continuous phase in these SIPNs contributes to the material mechanics. Furthermore, chemical gradients are applied to these systems through exposure to a competitive ligand, offering control over the localization of supramolecular interactions. These materials offer a framework to mediate mechanics while maintaining the ability to program gradient supramolecular interactions.

1. Introduction

In nature, materials exhibit complex behaviors through the organization of physical interactions, attaining structures afforded through a small chemical library of canonical amino acids paired with self-assembly. For example, polychaete worms exhibit Zinc-histidine (Zn-His) coordination crosslinks in their jaws, with a decreasing concentration of these interactions occurring down the length of the mandible [1,2]. The localization of these metal-ligand interactions contributes to changes in mechanical behavior along the jaw, yielding a single material displaying both stiff and soft material mechanics. Similarly, the byssus threads of marine mussels contain both Zn-His and catechol-Fe coordination interactions, which contribute to mechanical toughening and energy dissipation by behaving as reversible sacrificial bonds [2–4]. These interactions and their precise localization offer higher toughness and wear resistance than is typically achieved in conventional polymer materials.

To achieve similar sacrificial bond architectures and controllable interactions, researchers often turn to supramolecular chemistry to construct tunable, non-covalent assemblies. Supramolecular polymers offer a modular platform for tuning material toughness and architecture, with changes in mechanics and assembly being driven by both local environment and supramolecular connectivity. Much like the aforementioned mussel byssus threads, physical interactions in synthetic materials behave as sacrificial bonds, contributing to toughness by reversibly rupturing under deformation [5–7]. Another attractive aspect of supramolecular chemistries is their stimuli-responsive behavior, where the physical interactions can be modulated or disrupted by the presence of environmental changes, including heat [8], competitive solvents/ligands [8,9], ultraviolet (UV) light [10–12], and pH [13,14]. These characteristics have led to supramolecular-based materials seeing widespread use in drug delivery, tissue scaffolding, and sensing [15–17].

Of the many available interactions for building supramolecular polymer networks, metal-ligand coordination offers a convenient platform for constructing responsive, reinforced networks, due in part to the strength of their associations [17,18]. Moreover, these coordination interactions are sensitive to a number of stimuli, allowing for materials that can be mediated through changes in pH, the presence of competitive ligands, or shifts in coordinating metal chemistry [9,13,19]. Applying these strategies, bio-inspired materials that mimic the continuous gradients or mechanical enhancement present in natural systems have been realized. For example, Neal et al. utilized crosslinked acrylate networks bearing histidine residues to incorporate a continuous gradient into their films using a competitively binding solvent and concentration doping of a coordinating metal solution, resulting in controllable localized stiffness and coordination concentration [20]. To achieve high elasticity and toughness analogous to marine mussel

---

* Corresponding author at: 127 The Green, 309 DuPont Hall, Newark, DE 19716, USA.
E-mail address: lkorley@udel.edu (L.T.J. Korley).

https://doi.org/10.1016/j.eurpolymj.2019.04.015
Received 23 December 2018; Received in revised form 30 March 2019; Accepted 7 April 2019

byssal threads, Holten-Andserson et al. utilized catechol-functional hydrogels that could be crosslinked with Fe^{3+} [13]. The assembly of these gels were controlled by changes in pH and displayed storage modulus values that were similar to a covalently-crosslinked gel while maintaining self-healing properties.

Using supramolecular chemistry as a platform, we incorporate 2,6-bis(1′-methyl-benzimidazolyl)-4-hydroxypyridine (BIP) functionalized polymers into a supramolecular semi-interpenetrating network (SIPN) framework, wherein the covalent crosslinks confine the supramolecular interactions and offer a handle to tune the mechanics of the network. As a subset of polymer blends, semi-interpenetrating networks combine two or more polymer networks, at least one of them covalently crosslinked. The crosslinking process restricts phase separation that occurs in many polymer blends; the covalent crosslinks act as a barrier to macrophase separation and restrict the phases to the micron or sub-micron scale [21,22]. Interpenetrating networks containing supramolecular chemistry in one of the material phases have been recently applied to construct tough materials with applications in self-healing and tissue engineering [23–25]. This pathway allows for exploration of the chemoresponsive behaviors of BIP within a covalent matrix, independently tuning self-assembly and mechanics while maintaining a stable film. Using these SIPNs, we program gradients in Zn^{2+} metal concentration, and, thus, control the localization of metal-ligand coordination interactions. These systems offer supramolecular interaction localization and tunable mechanical responses.

2. Experimental

2.1. Materials

All chemicals were used as received unless stated otherwise. Chelidamic acid, tetrahydrofuran (anhydrous) and N-methylphenylenediamine were purchased from Acros Organics. Poly(ethylene glycol) dimethacrylate (PEGDMA, M_n ~750 g/mol), pentaerythritol tetrakis(3-mercaptopropionate) (PETMP), diethyl azodicarboxylate (DEAD, 40 wt % in toluene), triphenylphosphine (TPP), and 2,2-dimethoxy-2-phenylacetophenone (DMPA) were purchased from Sigma Aldrich. N,N,N',N'-tetramethylethylenediamine (TMEDA) was purchased from Alfa Aesar. Zinc(II)bis(trifluoromethanesulfonamide) ($Zn(NTf_2)_2$) was purchased from Strem Chemicals. Poly(ethylene-co-1-butene) (PEB) was generously donated by Nippon Soda Co. All other solvents and reagents were purchased from Fisher Scientific and used as received.

2.2. General characterization

Purification of synthesized reagents was carried out on a Teledyne ISCO CombiFlash RF Prep flash column purification system. ^1H Nuclear magnetic resonance (NMR) spectroscopy was performed on a Bruker 600 MHz NMR using 256 scans. After crosslinking the SIPN, the network structure was probed *via* Soxhlet extractions in chloroform. From Soxhlet, the extracted sol was measured, and the gel fraction was calculated using Eq. (1):

$$gel - sol \ \ fraction(\%) = 100 \times \left[1 - \left(\frac{m_i - m_f}{m_i}\right)\right] \tag{1}$$

where m_i and m_f are the initial and final masses of the extracted films, respectively [26].

Stress-strain experiments were conducted on a Zwick Roell fitted with a 100 N load cell operating in tension mode. A pre-load force of 0.005 N was applied before testing, and all tests were carried out at a strain rate of $10\%\text{min}^{-1}$ until failure. Samples for tensile testing were typically 3 mm wide and 0.2 mm thick with a gauge length between 5 and 10 mm. Crosslinked PEG controls had a sample thickness of 0.7 mm due to the difficulty of removing the more brittle PEG from the mold when cast as a thinner film. All samples were tested in triplicate to ensure reproducibility of the observed mechanical behaviors.

X-ray photoelectron spectroscopy (XPS) was carried out on a K-Alpha Series instrument from Thermo Fisher Scientific. Line scans were performed on films between 1.0 and 1.5 cm long, with scans taken down the length of the film using a beam size of 400 μm and a step size of 600 μm for each scan. Peak fitting and elemental analysis were done in Avantage software (Thermo Fisher Scientific). The data is reported as normalized peak area to denote the change in the amount of Zn^{2+} down the length of the film irrespective of the proportions of surrounding elements (e.g. C, N). This approach was chosen so that potential rearrangements of the supramolecular polymer during gradient formation wouldn't influence the amount of Zn^{2+} that was observed in the processed data.

Atomic force microscopy (AFM) was acquired on a Bruker Dimension 3100 V in tapping mode using Sb-doped Si tips (Bruker). Images were taken at a scan size of 5 μm with 512 scans and 512 points per line. Height and phase images were processed in the open-source Gwyddion software.

Scanning electron microscopy (SEM) was conducted on a JSM-7400F (Jeol) at an accelerating voltage of 3 kV. All samples were sputter-coated with a layer of Au/Pd prior to imaging. For fractography, samples were subjected to tensile testing up until failure prior to imaging. Images were gathered near the fracture edge of the films. To view the SIPN morphology, samples were extracted in chloroform overnight to remove the soluble BPEB-Zn, dried under vacuum, sputter-coated, and imaged.

SAXS data was acquired at the Advanced Materials Characterization Laboratory (AMCL) on a Xenocs Xeuss 2.0. The scattered beam was recorded on a CCD detector with a pixel resolution of 486 × 618 (1 pixel = 0.172 mm). The data collection time was 60 min. For the measurements, X-rays were generated at 50 kV/0.6 Ma at a beam wavelength of 1.542 Å (Cu Kα radiation) and sample-to-detector distances of 1200 cm. The instrument was calibrated using silver behenate. The generated X-ray beam was slit-collimated using a Kratky camera with a beam size of 0.3 mm (length) × 0.3 mm (width). The data was corrected for sample absorption and background noise before scaling to absolute intensity (cm^{-1}). The two-dimensional data sets were azimuthally averaged to give intensity as a function of the magnitude of the scattering vector, q, where $q = 4\pi\sin(\theta)/\lambda$ and 2θ is the scattering angle. All data processing and analysis was performed using Origin 8.8. Bragg diffraction maxima were fitted using a Lorentzian peak fitting function. For gradient samples, scattering was performed down the length of the sample to probe the structural shifts that occurred after exposure to the competitive TMEDA ligand; 5 measurements were taken and a step size of ~1 mm was used.

Nanoindentation was performed on a Nanoindenter XP (MTS) fitted with a Berkovich tip. Samples were mounted on double sided tape; care was taken to ensure that the samples were flat prior to testing. The sample surface was deformed to a depth of 2 μm, and a Poisson's ratio of 0.4 was used for all calculations. To compare how the gradient may impact local mechanics, indentations were performed down the length of a gradient SIPN-70 film. A step size of 1200 μm was applied between each indent and multiple spots were run per line. Due to surface roughness, it was difficult to retrieve triplicates of each indented line. This constraint limits quantitative analysis of the data; however, the general trend in elastic modulus can be used to highlight how local mechanics are changing down the length of the gradient film.

2.3. Synthesis of BPEB-Zn SIPN

BIP and BPEB-Zn were synthesized according to an established procedure [9,11]. BPEB-Zn was incorporated into the SIPN in varying weight percentages to probe the effects of increasing supramolecular polymer content on the resultant behavior of the SIPNs. To distinguish between different samples, the nomenclature SIPN-X was chosen, where X represents the weight percent (wt%) of BPEB-Zn present in the final film. The fabrication procedure for SIPN-50 is detailed as an example. To a round bottom flask, BPEB (0.49 g, 0.13 mmol) was dissolved in 5 mL of chloroform. $Zn(NTf_2)_2$ (56 mg, 8.9×10^{-2} mmol) was prepared as a 0.1 M solution in acetonitrile and added to the BPEB solution. The amount of $Zn(NTf_2)_2$ was chosen to achieve a ratio of 0.7:1 Zn^{2+}:BIP coordination sites (accounting for the 2:1 BIP:Zn^{2+} coordination structure). This stoichiometry was chosen based on results from Burnworth et al. where a slight excess of BIP contributed to enhanced mobility of free BIP units during light-driven healing experiments [11]. After allowing the $Zn(NTf_2)_2$ to dissolve, all solvents were removed under vacuum and the components were dissolved in 5 mL of chloroform.

In a separate flask, PEGDMA (0.37 g, 0.49 mmol), PETMP (0.12 g, 0.25 mmol), and DMPA (5 mg, 2.0×10^{-2} mmol) were dissolved in 5 mL of chloroform before addition to the flask containing BPEB-Zn. The solution was stirred briefly and cast into a trimethyl silane-treated petri dish, covered (to prevent the premature termination of photoinitiator), and allowed to anneal overnight prior to curing. In some cases, it was important to leave the cast films in a chloroform atmosphere for additional 24 hrs to promote the formation of an even film.

The films were cured in a UV chamber (SPDI UV, $\lambda = 365$ nm) for a total of 20 min (10 min exposure for each side of the film) at an intensity of ~ 11 mW/cm^2. After curing, the films were annealed in a vacuum oven at 80 °C for one day to remove any volatile compounds and to terminate any remaining initiator or acrylate functionalities. A similar procedure was used to produce PEG-based controls, consisting of PEGDMA crosslinked with stoichiometric amounts of PETMP.

2.4. Gradient structures in SIPN films

To impart localization of metal-ligand interactions into the films, we introduced a competitive ligand (TMEDA) as a pathway to achieve gradients in metal-ligand coordination interactions. Toward this goal, small lengths (1.0 – 1.5 cm) of film were suspended over a solution of TMEDA, with only their ends directly exposed to the ligand. The ligand was incorporated into the film *via* capillary action. The gradient properties were evaluated using XPS, SAXS, nanoindentation, and SEM fractography to track changes in Zn^{2+} localization and structural shifts of the BPEB-Zn, respectively.

3. Results and discussion

3.1. Material synthesis and film fabrication

The metallopolymer precursor (BPEB-Zn) was synthesized through a Mitsunobu coupling procedure (Fig. 1), yielding oligomeric, bifunctional chains that could be chain-extended through coordination of their BIP end-groups with $Zn(NTf_2)_2$. The Mitsunobu pathway was chosen due to the efficient coupling between the primary alcohol groups on the PEB termini and the relatively acidic phenol residue on BIP in the presence of TPP and DEAD [27]. The BIP and BPEB structures were characterized *via* ^{1}H NMR (Fig. S1). Coordinated BPEB-Zn was crosslinked into a PEG-based matrix through UV-driven thiol-radical click addition (Fig. 1). The formation of an orthogonal crosslinked PEG network was utilized to shift the phase behavior of the SIPN films and to result in a platform to tune the mechanical behavior. By increasing the wt% of BPEB-Zn from (30, 50 and 70 wt%), the size of phase domains and character of the continuous network were controlled, moving from a system in which PEG formed the continuous network (SIPN-30 and SIPN-50) toward a system where the BPEB-Zn formed the continuous phase (SIPN-70). This design strategy provided an avenue for probing the interplay between covalent crosslinking and supramolecular interactions in an orthogonally-bound SIPN framework, and the mechanical, morphological, and stimuli-responsive behavioral shifts that occurs with increasing BPEB-Zn content. The use of UV-initiated thiol-radical click chemistry was chosen due to its high efficiency, as evidenced by the high gel fractions achieved for each film (Table S1).

3.2. Mechanical characterization and morphology

The mechanics of the supramolecular SIPN films were probed by tensile testing, wherein each film was subjected to deformation until failure (Fig. 2). It is initially apparent that the crosslinked PEG control shows a linear deformation typical of conventional elastomers, while also exhibiting limited extensibility (~19%) and, thus, limited toughness. This behavior can be attributed to the tightly crosslinked network that is being formed by the short PEGDMA chains ($M_n \sim 750$ g/mol). Additionally, while it is expected that thiol-methacrylate coupling is the primary mechanism for crosslinking in these materials, radical polymerization between methacrylate groups cannot be ruled out; such crosslinks could contribute to the brittle behavior observed in these systems.

The BPEB-Zn system shows the highest extensibility and toughness of the tested films, which can be attributed to the supramolecular organization, wherein the BIP-Zn coordination sites act as sacrificial bonds, dissipating absorbed energy by rupturing during deformation, a primary toughening mechanism in supramolecular polymer networks [5,28,29]. These metal-ligand coordination interactions in the supramolecular BPEB-Zn also lead to toughness enhancement of the PEG crosslinked network in the SIPN samples. In SIPN-50 and SIPN-70, it is apparent that, while the BPEB-Zn plays a large role in the improved toughness of these materials, their extensibility is still limited by the covalent matrix. In both of these samples, a quasi-linear deformation behavior is observed until film failure. Interestingly, SIPN-30 displays higher extensibility and toughness than the other two SIPN samples at a lower BPEB-Zn content. Whereas SIPN-50 and SIPN-70 display a quasi-linear yield up until failure, SIPN-30 exhibits a yield point indicative of more plastic-like deformation. In particular, such behaviors are observable in rubber-reinforced plastic materials, alleviating the brittleness of the continuous phase (PEG in this case) [30,31].

Examining the fractured film surfaces under SEM (Fig. 3) offers insight into the deformation behavior and energy dissipation pathways that are present in the controls (PEG and BPEB-Zn) and the SIPN series. For PEG, the formation and propagation of microcracks is the primary pathway for alleviating stress, indicative of a more brittle material deformation behavior [32,33]. In contrast, BPEB-Zn shows evidence of cavitation, an important means of energy dissipation supported by the plateau region visible in the tensile curves of BPEB-Zn, where the growth of these voids led to a decrease in the stress response of the material up until failure [34].

These findings frame analysis of the supramolecular SIPN films. SIPN-30 exhibits similar cavitation as seen in BPEB-Zn, where the growth of voids serves to alleviate stress at failure zones. These cavitation events are represented in the tensile curve by the plateau region that occurs after the sample yields, contributing to the sample's high toughness when compared to other SIPN samples. Interestingly, these cavities are not present in SIPN-50, where the sample again exhibits microcracking that explains the brittle failure of the sample at relatively low strains (~47%). SIPN-70 shows some evidence of cavitation events during deformation, but these voids appear less often than in SIPN-30 and BPEB-Zn samples, which supports the more brittle fracture mechanism observed.

To better understand the interactions between the phases in our SIPNs that dictate the mechanical behavior, atomic force microscopy (AFM) and SEM were utilized to probe the phase separation occurring within the SIPN systems (Figs. 4, S3). As expected, increasing the BPEB-Zn content in the system increases the phase size, eventually resulting in a phase inversion in SIPN-70, where BPEB-Zn and PEG form a co-continuous network. Interestingly, there is no co-continuous morphology accessed at a 50/50 ratio of PEG/BPEB-Zn, which might be expected when the network constituents are present in equal amounts. Instead, BPEB-Zn is present in dispersed droplets. Inspecting extracted

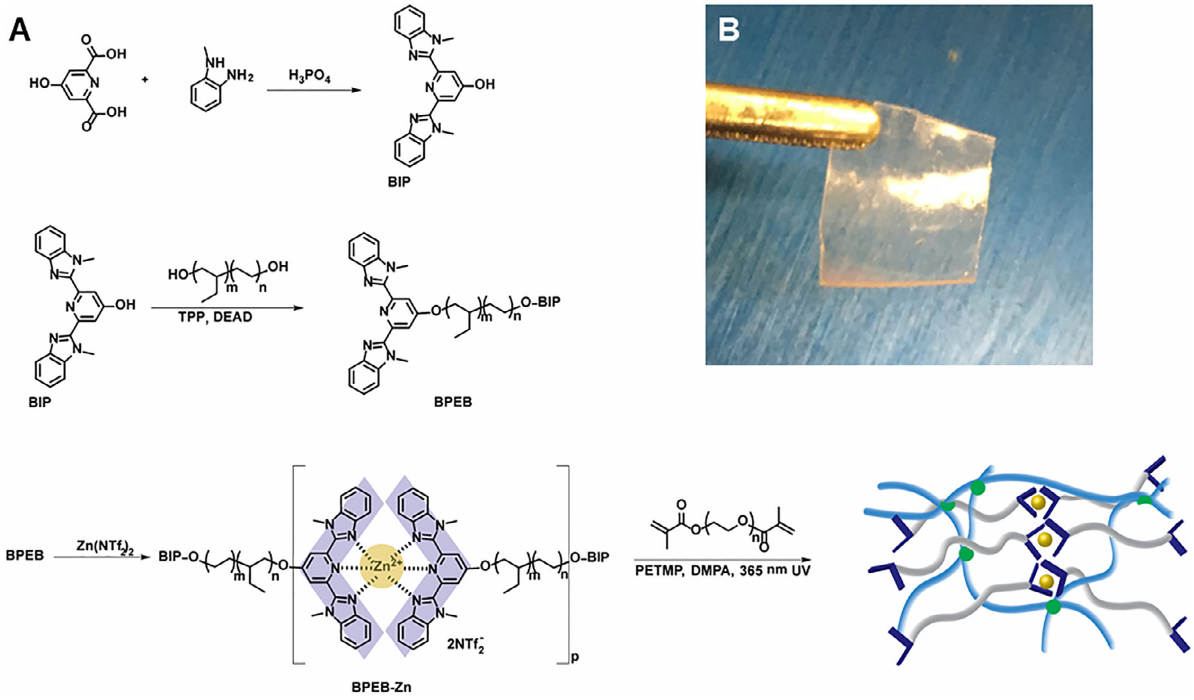

Fig. 1. (A) Synthesis scheme of BPEB-Zn and SIPNs. Here, the blue lines and green nodes represent the PEGDMA chains and PETMP crosslink junctions, respectively. (B) Photograph of SIPN-70 film. (For interpretation of the references to colour in this figure legend, the reader is referred to the web version of this article.)

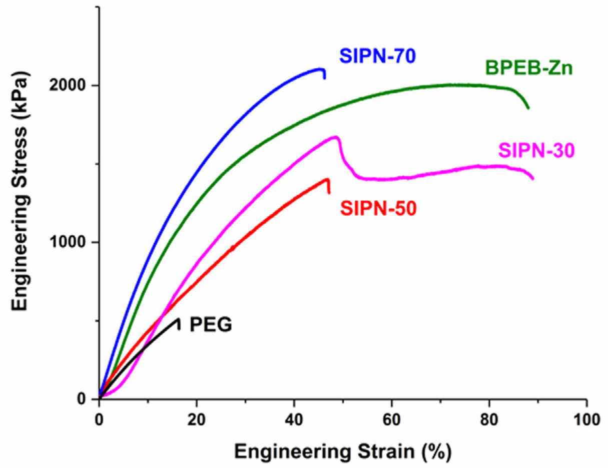

	E_t (MPa)	ε_B (%)	σ_m (MPa)	Toughness (MJ/m^3)
PEG	3.16 ± 0.24	19.2 ± 6.16	0.55 ± 0.15	0.06 ± 0.03
BPEB-Zn	8.54 ± 0.82	88.4 ± 16.7	1.99 ± 0.04	1.37 ± 0.28
SIPN-30	4.63 ± 0.61	66.1 ± 17.1	1.48 ± 0.16	0.76 ± 0.30
SIPN-50	4.12 ± 0.15	46.5 ± 5.10	1.37 ± 0.06	0.38 ± 0.06
SIPN-70	7.73 ± 0.97	46.8 ± 2.58	1.89 ± 0.19	0.60 ± 0.07

Fig. 2. Tensile behavior of the SIPN systems and controls. The table summarizes Young's modulus (E_t), strain-at-break (ε_b), maximum stress (σ_m), and toughness values.

SEM images initially shows evidence of rather large droplet formations, but the AFM results point to what appears to be smaller, irregular droplets. This morphological analysis suggests that a co-continuous morphology may have formed initially, but the tightly crosslinked covalent network drove break-up into droplets to minimize interactions between the incompatible networks [35]. However, the breakup of co-continuous phases would leave areas rich and poor in supramolecular polymer. Upon extraction with chloroform, the removal of BPEB-Zn from the areas rich in supramolecular polymer could cause the remaining PEG to contract. This hypothesis is supported in part by the porous structure of the extracted regions (Fig. S4), indicating smaller droplet formations being removed from the material during extraction.

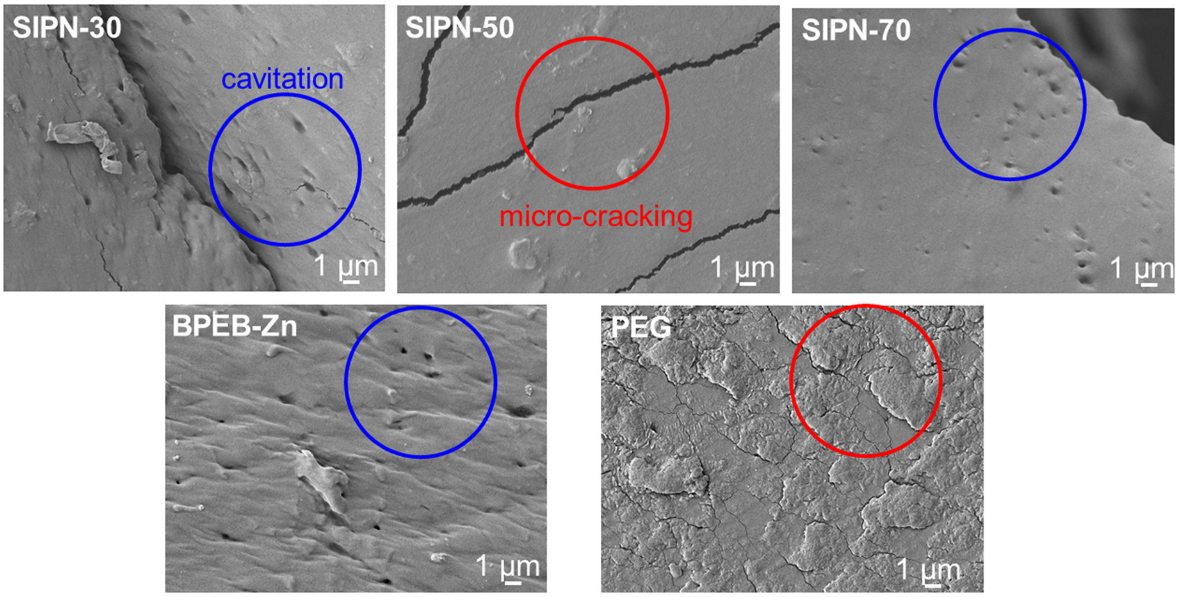

Fig. 3. SEM images of fractured SIPN, BPEB-Zn, and PEG samples highlighting the presence of cavitational voids (BPEB-Zn, SIPN-30, SIPN-70) and microcracks (PEG, SIPN-50) upon sample failure.

These results agree well with data derived from tensile testing, wherein a primarily linear deformation is observed in the SIPN-50 sample, alluding to the covalently crosslinked PEG phase dominating the deformation of the sample due to it forming the continuous network. The co-continuity accessed by SIPN-70 is also likely driven by the tightly crosslinked network; while present in smaller amounts than the BPEB-Zn, the high crosslinking efficiency driven by the use of thiol-radical "click" addition allows for the crosslinked PEG to still span the network. This behavior is well supported by the tensile data since the SIPN-70 curve shows a blend of both PEG brittle deformation and a discrete yield directly before failure occurs. The small droplets in SIPN-30 are reminiscent of droplet dispersions that are present in rubber-toughened polymer blends, where the droplets act as energy absorption and dissipation centers, serving to prevent catastrophic failure and crack propagation [30,32,34]. It is proposed that the BPEB-Zn droplet phase in SIPN-30 plays a similar role in toughening the brittle PEG continuous phase. However, while SIPN-50 shows the same droplet morphology, it lacks the plastic yielding of SIPN-30. This behavior could be partially explained by the droplet size and distribution. The droplets formed by SIPN-30 are smaller and distributed more evenly, driving more local deformation of the supramolecular phase and more energy dissipation events, a behavior noted in some rubber-toughened polymer blends [31,33,36].

To understand how the crosslinking of the PEG matrix impacts the organization of supramolecular motifs in the SIPNs, SAXS was utilized to determine if confinement of the BPEB-Zn by a crosslinked network shifts BPEB-Zn assembly. The 1-dimensional (1D) scattering patterns of the SIPN films show that the BPEB-ZN forms microphase-separated lamellar morphologies in which the metal-ligand complexes form a 'hard phase' that physically crosslinks the poly(ethylene-co-butylene) 'soft' domains (Fig. 5) [11]. The SAXS data highlights ordered, lamellar diffraction patterns with a strong Bragg diffraction maximum at integer multiples of the primary diffraction peak (2q*, 3q*, and above). The long-range ordering of the SIPN-X materials increases as the weight percentage of BPEB-Zn in the SIPN is increased (9.15 for SIPN-30 to 9.84 nm for SIPN-70), consistent with local confinement of metal-ligand coordination interactions caused by the presence of covalent crosslinks in the SIPN films with less BPEB-Zn. However, SIPN-70 displayed extensive peak broadening when compared to other samples, indicating a disruption of the local ordering of the metal-ligand coordination assemblies caused by the presence of the PEG domains. This disruption is explained in part by the co-continuous morphology that is accessed at this weight ratio of the two phases. The reduced interfacial curvature and, therefore, forced interactions that occur between the two phases allow PEG to play a larger role in impacting the local ordering that is present in the BPEB-Zn phase. This behavior further supports the reduction in strain-at-break in the SIPN-70 sample during deformation, where the disruption of the metal-ligand coordination by the PEG

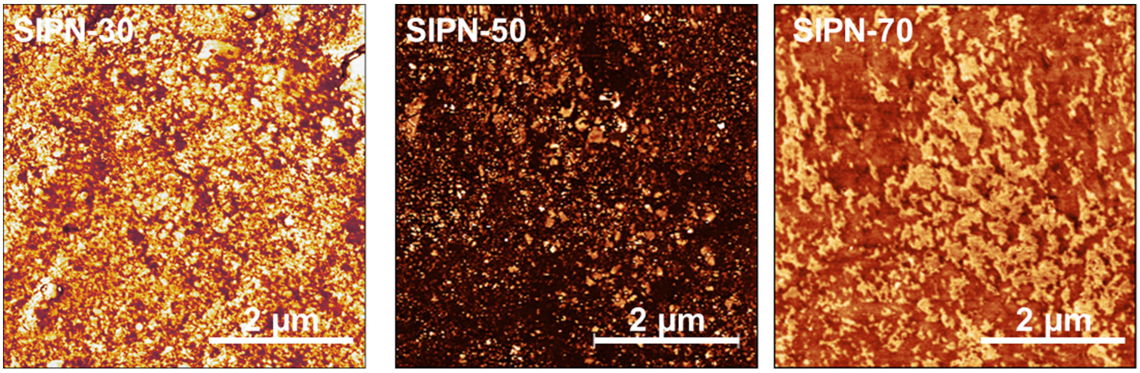

Fig. 4. AFM phase micrographs of SIPN samples SIPN-30 and SIPN-50 show dispersed droplets with distribution and size dictated by the ratio of BEPB-Zn present and the crosslink density of the PEG phase. SIPN-70 displays a co-continuous morphology.

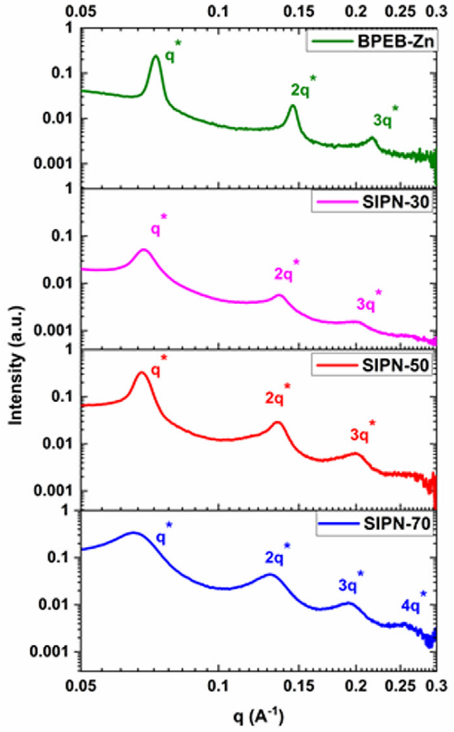

Sample	q* (1/Å)	Mean q*(1/Å)	Lamellar period (nm)	Peak width
BPEB-Zn	0.073	0.073	8.63	0.003
SIPN-30	0.069	0.069	9.15	0.007
SIPN-50	0.068	0.068	9.26	0.007
SIPN-70	0.065	0.064	9.84	0.019

Fig. 5. SAXS of SIPN and BPEB-Zn samples (top) and a table displaying q*, lamellar period, and peak width data (bottom).

network likely prevents effective energy dissipation prior to failure.

3.3. Gradient formation in SIPN films

Polychaete worms derive the strength in their jaws from gradient metal-ligand interactions, resulting in a mandible with a remarkable ability to absorb and dissipate energy by exhibiting a hard, energy absorptive phase at the tip of the jaw and an energy dissipating, soft material near the jaw's base [1,2]. In an effort to mimic the gradient structures present in these worm jaws, the end of SIPN films were exposed to a competitive TMEDA ligand for 60 s and gradients were programmed into the films through capillary action (the setup for incorporating gradients is pictured in Fig. S6). The gradients were visualized by XPS and SAXS, wherein the amount of Zn^{2+} present in different areas of the film demonstrates the ability for generation of gradients in these through the presence of a competitive ligand.

It is apparent from the normalized peak curves derived from XPS (Fig. 6) that the gradient behavior in each film shifts between SIPN samples. In SIPN-30, a minimum in Zn^{2+} is seen before a maximum is reached by the 5th position (3000 μm from the film's edge) after a gradual increase in Zn^{2+} concentration. The decrease in Zn^{2+} further down the length of the film could be caused by concentration of the Zn^{2+} at the TMEDA solvent front, where the droplet-in-matrix morphology of SIPN-30 traps the localized Zn^{2+} after removal of the TMEDA. SIPN-70 shows a similar behavior to SIPN-30, however, the initial minimum in Zn^{2+} is extended, a behavior that can be attributed to the continuous BPEB-Zn phase. In this case, the diffusion of Zn^{2+} is not hindered by confinement to droplets. Contrastingly, SIPN-50 shows a more gradual increase in Zn^{2+} down the length of the film. The relatively slow increase in Zn^{2+} shown in this sample may be caused by both the isolated droplets and fluctuation in BPEB-Zn that occurs through the material after collapse of the co-continuous network during crosslinking of the PEG. With a larger interparticle distance between these droplets, movement of the Zn^{2+} may be hindered during TMEDA

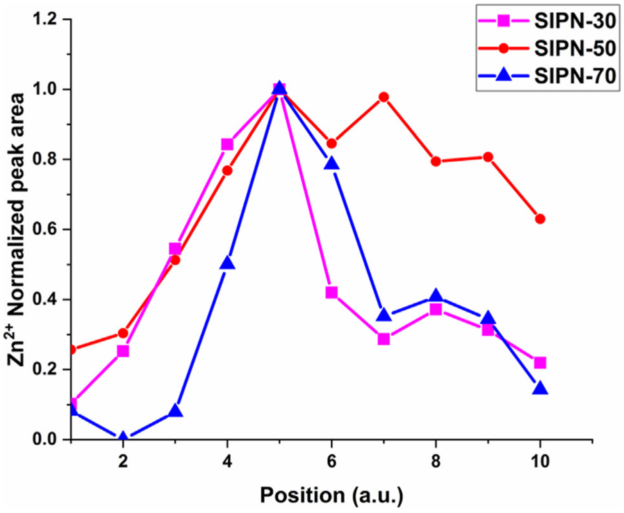

Fig. 6. Normalized peak area of the Zn^{2+} peak as derived from XPS. Each position denotes a 600 μm step size down the length of the film.

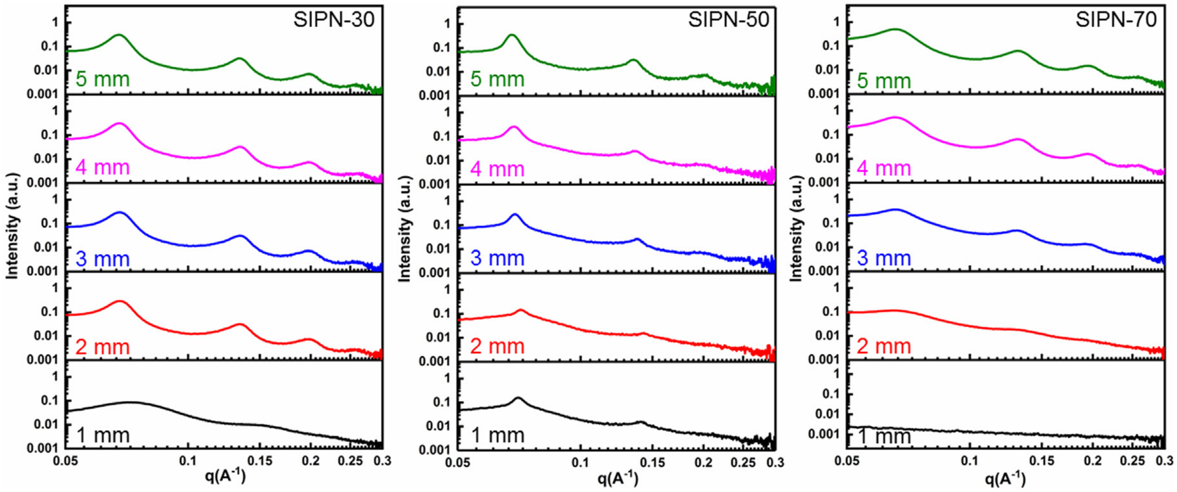

Fig. 7. SAXS data showing structural evolution of SIPNs upon exposure to TMEDA where that curves at 1 mm refer to the measurement taken nearest the end exposed to TMEDA.

travel.

To understand how the assembly of the BIP groups shifts during the application of the chemical gradient, SAXS measurements were taken down the length of the gradient films (Fig. 7). The derived data complements the XPS normalized peak area curves. In SIPN-30, the initial position displays a decrease in peak intensity and peak broadening, indicating a more disordered assembly that is reminiscent of the uncoordinated BPEB scattering peaks (Fig. S7); this disorder is also accompanied by a higher q^* value of 0.072 A^{-1} (Table S2). Further from the exposed end of the film, the curves match those of neat SIPN-30 and the q value decreases to 0.068 A^{-1}, where it stays relatively constant continuing down the length of the film. Furthermore, the peaks become narrower, indicating a more ordered structure that is synonymous with the presence of Zn^{2+} driving the assembly of coordinated structures. Conversely, SIPN-50 shows only a slight shift to higher q* values (0.070 A^{-1}) near the TMEDA-exposed film end, which is consistent with the XPS data where there is a more gradual change in Zn^{2+} concentration down the length of the film. In SIPN-70, the initial SAXS data near the exposed end of the film shows no appearance of scattering peaks. This behavior indicates a complete removal of BPEB. Since the BPEB-Zn acts as a continuous phase in these materials, the presence of TMEDA could have dissolved and extracted the BPEB-Zn in this area of the film. Moving down the film, the q* value remains consistent at 0.66 A^{-1}, but the peaks become narrower indicating an increase in local ordering.

To demonstrate how these changes in local structure in the SIPN films could change mechanics, the SIPN-70 gradient sample was subjected to nanoindentation (Fig. 8A). However, due to the surface roughness in these films, it was difficult to obtain multiple data points in every area of the film to consistently track changes in local modulus. For this reason, the obtained nanoindentation data is used more to showcase the trend of elastic modulus down the length of the film. The values obtained for local elastic modulus are also higher than expected when compared to bulk Young's modulus values; however, this trend can be explained by the use of the Berkovich tip for indenting, which has been shown to give higher values of elastic modulus when small indents are made [37]. Gratifyingly, the measured modulus at areas nearest the exposed end of the SIPN-70 film is significantly lower than the modulus measured for the SIPN-70 control (60 ± 11 MPa). This value increases as the indents are made further from the exposed film end, eventually showing close agreement with the measured local modulus of the neat SIPN-70 film, and indicating that the removal of Zn^{2+} influences changes in mechanical behavior. Due to the low molecular weight of the BPEB polymer, once the coordinating metal center is removed the oligomeric chains are unable to contribute greatly to the mechanical response of the sample.

The changes in local modulus were then compared to changes in the fracture behavior of the film. As stated above, the neat SIPN-70 films show evidence of cavitation events during defromation. SIPN-70 gradient samples were subjected to tensile testing and their fractured ends were observe to track how the change local structure may influence changes in energy dissipation (Fig. 8B, 8C). Interestingly, the bulk mechanical properties of the gradient SIPN-70 sample do not differ greatly from the neat SIPN-70 samples; however, slight reductions in strain-at-break and toughness are apparent (Table S4). Inspection of the fracture end shows evidence of microcracking as the primary pathway for energy dissipation, indicating that the brittle covalent PEG network is responsible for absorbing and dissipating the applied energy (Fig. 8B). Moving approximately 1 mm away from the fractured end of the film (~3 mm from the end of film prior to fracture), cavitational voids are observed on the film's surface (Fig. 8C). This voiding indicates that the supramolecular polymer is contributing to the energy dissipation events in this area of the film due to a higher concentration of Zn^{2+} than what is present near the fractured area of the film. This observed behavior is in good agreement with nanoindentation, SAXS, and XPS results that point to an increased concentration of Zn^{2+} metal centers 3 mm from the TMEDA-exposed end of the film.

3.4. Conclusions

Here, SIPNs were explored as a platform for generating materials with tunable mechanics dictated by their morphology and the local assembly of supramolecular motifs. SIPN-30 displayed the highest toughness of the SIPN samples. This behavior was attributed to the small droplets dispersed in the PEG matrix, shifting the deformation behavior to mimic that of a rubber-reinforced plastic material. Furthermore, this mechanical shift was supported by cavitation of SIPN-30 during deformation, as opposed to the formation of microcracks as viewed in SIPN-50. In an effort to mimic the gradient of metal-ligand coordination crosslinks exhibited by polychaete worms, a competitive ligand (TMEDA) was introduced into the SIPN films via capillary action to encourage the formation of Zn^{2+} gradients down the length of the film. The formation of the gradients was shown to be a function of the SIPN morphology. In SIPN-30 and SIPN-70, dramatic increases in Zn^{2+} occurred near the TMEDA-exposed end of the film, likely caused by the close distribution of droplets in the SIPN-30 system and continuous BPEB-Zn phase in SIPN-70. However, SAXS data indicated that there was removal of BPEB-Zn near the TMEDA-exposed end in SIPN-70 due

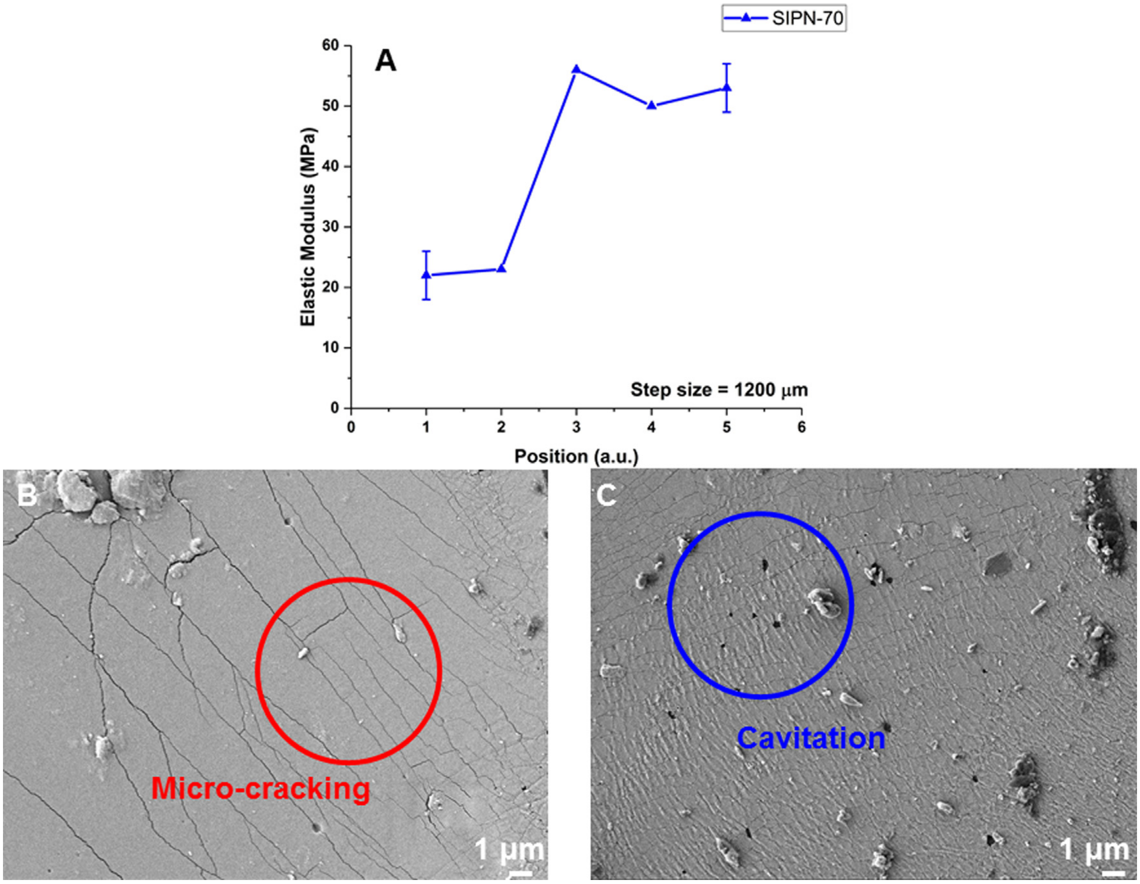

Fig. 8. (A) Nanoindentation data of SIPN-70 showing the change in measured modulus down the length of the film. (B) SEM image of the SIPN-70 gradient sample fracture edge after tensile testing to failure. (C) Evidence of cavitation events in the SIPN-70 gradient sample approximately 3 mm from the TMEDA-exposed end of the film.

in part to the co-continuous morpholgy exhibited in that sample. SIPN-50 showed a gradual increase in Zn^{2+} content down the length of the film; this behavior can be partially explained by the distribution of large droplets of BPEB-Zn in the PEG matrix resulting in a slower diffusion of Zn^{2+} up the length of the film. Furthermore, how changes in local structure impacted local mechanics was explored. Nanoindentation data indicated a trend of increasing modulus down the length of the gradient film in good agreement with the changes in structure noted in XPS and SAXS. This change in local stiffness was further supported by SEM fractography images, wherein microcracking dominated the energy dissipation pathway near the fracture end. This work showcased the ability to tune mechanics and stimuli-responsive behavior in a series of metal-ligand SIPN systems. The ability to control the localization of supramolecular interactions shows potential in the development of smart materials, including in the fields of biomaterials and sensing.

Acknowledgements

This work was supported by the National Science Foundation (NSF, DMR 1608441; NSF, OISE 1844463). Access to the XPS was supported by the NSF (MRI-1428149). The authors would also like to thank the research group of Prof. S. J. Rowan for helpful discussions and synthetic protocols for BIP and BPEB. Access to the SAXS was provided by the Advanced Materials Characterization Laboratory (AMCL) at the University of Delaware. Access to the AFM and SEM was provided by the Keck Microscopy Center at the University of Delaware. The authors would like to thank Babak Anasori and the Core Research Facilities (C.R.F.) at Drexel University for assistance with nanoindentation. The authors would like to thank the research group of Prof. C. J. Kloxin for access to the Teledyne ISCO CombiFlash RF flash column purification system.

The authors declare no competing financial interest.

The raw/processed data required to reproduce these findings cannot be shared at this time as the data also forms part of an ongoing study.

Appendix A. Supplementary material

Supplementary data to this article can be found online at https://doi.org/10.1016/j.eurpolymj.2019.04.015.

References

[1] H.C. Lichtenegger, T. Schö, J.T. Ruokolainen, J.O. Cross, S.M. Heald, H. Birkedal, J.H. Waite, G.D. Stucky, K.N. Raymond, Zinc and mechanical prowess in the jaws of Nereis, a marine worm, Proc. Natl. Acad. Sci. 100 (2003) 9144–9149.

[2] E. Degtyar, M.J. Harrington, Y. Politi, P. Fratzl, The mechanical role of metal ions in biogenic protein-based materials, Angew. Chemie Int. Ed. 53 (2014) 12026–12044, https://doi.org/10.1002/anie.201404272.

[3] E. Vaccaro, J.H. Waite, Yield and post-yield behavior of mussel Byssal thread: a self-healing biomolecular material, Macromolceules 2 (2001) 906–911, https://doi.org/10.1021/bm0100514.

[4] C.N.Z. Schmitt, Y. Politi, A. Reinecke, M.J. Harrington, Role of sacrificial protein – metal bond exchange in mussel Byssal thread self-healing, Biomacromolecules 16 (2015) 2852–2861, https://doi.org/10.1021/acs.biomac.5b00803.

[5] J. Yang, M. Ma, X. Zhang, F. Xu, Elucidating dynamics of precoordinated ionic bridges as sacrificial bonds in interpenetrating network hydrogels, Macromolecules 49 (2016) 4340–4348, https://doi.org/10.1021/acs.macromol.6b00874.

[6] T.L. Sun, F. Luo, W. Hong, K. Cui, Y. Huang, H.J. Zhang, D.R. King, T. Kurokawa, T. Nakajima, J.P. Gong, Bulk energy dissipation mechanism for the fracture of tough and self-healing hydrogels, Macromolecules 50 (2017) 2923–2931, https://doi.org/10.1021/acs.macromol.7b00162.

[7] S. Shinde, J.L. Sartucci, D.K. Jones, N. Gavvalapalli, Dynamic π-conjugated polymer

ionic networks, Macromolecules 50 (2017) 7577–7583, https://doi.org/10.1021/acs.macromol.7b01896.

[8] J. Sautaux, L. Montero De Espinosa, S. Balog, C. Weder, Multistimuli, multi-responsive fully supramolecular orthogonally bound polymer networks, Macromolecules 51 (2018) 5867–5874, https://doi.org/10.1021/acs.macromol.8b00555.

[9] S.J. Rowan, J.B. Beck, Metal-ligand induced supramolecular polymerization: a route to responsive materials, Faraday Discuss 128 (2005) 43–53, https://doi.org/10.1039/B403135K.

[10] J.R. Kumpfer, S.J. Rowan, Thermo-, photo-, and chemo-responsive shape-memory properties from photo-cross-linked metallo-supramolecular polymers, J. Am. Chem. Soc. 133 (2011) 12866–12874, https://doi.org/10.1021/ja205332w.

[11] M. Burnworth, L. Tang, J.R. Kumpfer, A.J. Duncan, F.L. Beyer, G.L. Fiore, S.J. Rowan, C. Weder, Optically healable supramolecular polymers, Nature 472 (2011) 334–337, https://doi.org/10.1038/nature09963.

[12] S. Coulibaly, A. Roulin, S. Balog, M.V. Biyani, E.J. Foster, S.J. Rowan, G.L. Fiore, C. Weder, Reinforcement of optically healable supramolecular polymers with cellulose nanocrystals, Macromolecules 47 (2014) 152–160, https://doi.org/10.1021/ma402143c.

[13] N. Holten-Andersen, M.J. Harrington, H. Birkedal, B.P. Lee, P.B. Messersmith, K. Yee, C. Lee, J.H. Waite, pH-induced metal-ligand cross-links inspired by mussel yield self-healing polymer networks with near-covalent elastic moduli, Proc. Natl. Acad. Sci. 108 (2011) 2651–2655, https://doi.org/10.1073/pnas.1015862108/-/DCSupplemental.

[14] S.C. Grindy, N. Holten-Andersen, Bio-inspired metal-coordinate hydrogels with programmable viscoelastic material functions controlled by longwave UV light, Soft Matter. 13 (2017) 4057–4065, https://doi.org/10.1039/c7sm00617a.

[15] C.B. Thompson, L.T.J. Korley, Harnessing supramolecular and peptidic self-assembly for the construction of reinforced polymeric tissue scaffolds, Bioconjug. Chem. 28 (2017) 1325–1339, https://doi.org/10.1021/acs.bioconjchem.7b00115.

[16] D. Knapton, M. Burnworth, S.J. Rowan, C. Weder, Fluorescent organometallic sensors for the detection of chemical-warfare-agent mimics, Angew. Chemie 118 (2006) 5957–5961, https://doi.org/10.1002/ange.200601634.

[17] E.A. Appel, J. del Barrio, X.J. Loh, O.A. Scherman, Supramolecular polymeric hydrogels, Chem. Soc. Rev. 41 (2012) 6195–6214, https://doi.org/10.1039/c2cs35264h.

[18] S.-L. Li, T. Xiao, C. Lin, L. Wang, Advanced supramolecular polymers constructed by orthogonal self-assembly, Chem. Soc. Rev. 41 (2012) 5950–5968, https://doi.org/10.1039/c2cs35099h.

[19] X.-Y. Hu, T. Xiao, C. Lin, F. Huang, L. Wang, Dynamic supramolecular complexes constructed by orthogonal self-assembly, Acc. Chem. Res. 47 (2014) 2041–2051, https://doi.org/10.1021/ar5000709.

[20] J.A. Neal, N.J. Oldenhuis, A.L. Novitsky, E.M. Samson, W.J. Thrift, R. Ragan, Z. Guan, Large continuous mechanical gradient formation via metal-ligand interactions, Angew. Chemie. 129 (2017) 15781–15785, https://doi.org/10.1002/ange.201707587.

[21] Y.S. Lipatov, T.T. Alekseeva, Phase-Separated Interpenetrating Polymer Networks, Adv. Polym. Sci., Springer, 2007, p. 218.

[22] T. Trakulsujaritchok, D.J. Hourston, Damping characteristics and mechanical properties of silica Wlled PUR/PEMA simultaneous interpenetrating polymer networks, Eur. Polym. J. 42 (2006) 2968–2976, https://doi.org/10.1016/j.eurpolymj.2006.07.028.

[23] E.M. Foster, E.E. Lensmeyer, B. Zhang, P. Chakma, J.A. Flum, J.J. Via, J.L. Sparks, D. Konkolewicz, Effect of polymer network architecture, enhancing soft materials using orthogonal dynamic bonds in an interpenetrating network, ACS Macro Lett. (2017) 495–499, https://doi.org/10.1021/acsmacrolett.7b00172.

[24] J.-Y. Sun, X. Zhao, W.R.K. Illeperuma, O. Chaudhuri, K.H. Oh, D.J. Mooney, J.J. Vlassak, Z. Suo, Highly stretchable and tough hydrogels, Nature 489 (2012) 133–136, https://doi.org/10.1038/nature11409.

[25] M.M. Fitzgerald, K. Bootsma, J.A. Berberich, J.L. Sparks, Tunable stress relaxation behavior of an alginate-polyacrylamide hydrogel: comparison with muscle tissue, Biomacromolecules 16 (2015) 1497–1505, https://doi.org/10.1021/bm501845j.

[26] L. Matolyak, J. Keum, L.T.J. Korley, Molecular design: network architecture and its impact on the organization and mechanics of peptide-polyurea hybrids, Biomacromolecules 17 (2016) 3931–3939, https://doi.org/10.1021/acs.biomac.6b01309.

[27] L. Kurti, B. Czako, Strategic Applications of Named Reactions in Organic Syntheis, Elsevier Academic Press, 2005.

[28] S. Monemian, L.T.J. Korley, Exploring the role of supramolecular associations in mechanical toughening of semi-interpenetrating polymer networks, Macromolecules 48 (2015) 7146–7155, https://doi.org/10.1021/acs.macromol.5b01752.

[29] B.J. Gold, C.H. Hövelmann, C. Weiss, A. Radulescu, J. Allgaier, W. Pyckhout-Hintzen, A. Wischnewski, D. Richter, Sacrificial bonds enhance toughness of dual polybutadiene networks, Polymer 87 (2016) 123–128, https://doi.org/10.1016/J.POLYMER.2016.01.077.

[30] C.B. Bucknall, Quantitative approaches to particle cavitation, shear yielding, and crazing in rubber-toughened polymers, J. Polym. Sci. Part B Polym. Phys. 45 (2007) 1399–1409, https://doi.org/10.1002/polb.21171.

[31] A. Van Der Wal, A.J.J. Verheul, R.J. Gaymans, Polypropylene-rubber blends: 4. The effect of the rubber particle size on the fracture behaviour at low and high test speed, Polymer 40 (1999) 6057–6065.

[32] S. Monemian, L.T.J. Korley, Exploring the role of supramolecular associations in mechanical toughening of interpenetrating polymer networks, Macromolecules 48 (2015) 7146–7155, https://doi.org/10.1021/acs.macromol.5b01752.

[33] K. Wang, L. Chen, J. Wu, Mei L. Toh, C. He, A.F. Yee, Epoxy nanocomposites with highly exfoliated clay: mechanical properties and fracture mechanisms, Macromolecules (2005), https://doi.org/10.1021/ma048465n.

[34] O. Lopez-Pamies, M.I. Idiart, T. Nakamura, Cavitation in elastomeric solids: I—a defect-growth theory, J. Mech. Phys. Solids 59 (2011) 1464–1487, https://doi.org/10.1016/J.JMPS.2011.04.015.

[35] A.A. Donatelli, L.H. Sperling, D.A. Thomas, Interpenetrating polymer networks based on SBR/PS. 1. Control of morphology by level of cross-linking, Macromolecules 9 (1976) 671–675, https://doi.org/10.1021/ma60052a029.

[36] S. Wu, Impact fracture mechanisms in polymer blends: rubber-toughened nylon, J. Polym. Sci. Polym. Phys. Ed. 21 (1983) 699–716, https://doi.org/10.1002/pol.1983.180210503.

[37] C.-S. Han, S.H.R. Sanei, F. Alisafaei, On the origin of indentation size effects and depth dependent mechanical properties of elastic polymers, J. Polym. Eng. 36 (2016) 103–111, https://doi.org/10.1515/polyeng-2015-0030.